UC Santa Barbara

UC Santa Barbara Previously Published Works

Title

Enzymatic degradation of liquid droplets of DNA is modulated near the phase boundary

Permalink

https://escholarship.org/uc/item/1x91j99b

Journal

Proceedings of the National Academy of Sciences of the United States of America, 117(28)

ISSN

0027-8424

Authors

Saleh, Omar A
Jeon, Byoung-jin
Liedl, Tim

Publication Date

2020-07-14

DOI

10.1073/pnas.2001654117

Peer reviewed

eScholarship.org Powered by the California Digital Library
University of California

Enzymatic degradation of liquid droplets of DNA is modulated near the phase boundary

Omar A. Saleh[a,1], Byoung-jin Jeon[a], and Tim Liedl[b]

[a]Materials Department, University of California, Santa Barbara, CA 93106; and [b]Physics Department, Ludwig-Maximilians University, 80539 Munich, Germany

Edited by David A. Weitz, Harvard University, Cambridge, MA, and approved May 31, 2020 (received for review January 30, 2020)

Biomolecules can undergo liquid–liquid phase separation (LLPS), forming dense droplets that are increasingly understood to be important for cellular function. Analogous systems are studied as early-life compartmentalization mechanisms, for applications as protocells, or as drug-delivery vehicles. In many of these situations, interactions between the droplet and enzymatic solutes are important to achieve certain functions. To explore this, we carried out experiments in which a model LLPS system, formed from DNA "nanostar" particles, interacted with a DNA-cleaving restriction enzyme, SmaI, whose activity degraded the droplets, causing them to shrink with time. By controlling adhesion of the DNA droplet to a glass surface, we were able to carry out time-resolved imaging of this "active dissolution" process. We found that the scaling properties of droplet shrinking were sensitive to the proximity to the dissolution ("boiling") temperature of the dense liquid: For systems far from the boiling point, enzymes acted only on the droplet surface, while systems poised near the boiling point permitted enzyme penetration. This was corroborated by the observation of enzyme-induced vacuole-formation ("bubbling") events, which can only occur through enzyme internalization, and which occurred only in systems poised near the boiling point. Overall, our results demonstrate a mechanism through which the phase stability of a liquid affects its enzymatic degradation through modulation of enzyme transport properties.

biomolecular liquid | coacervate | DNA self-assembly | restriction enzyme | liquid–liquid phase separation

Solutions of mutually attractive macromolecules can undergo a liquid–liquid phase-separation (LLPS) process that creates a coexistence between two phases that are, respectively, dense and sparse in macromolecule. The macromolecular LLPS process, also known as coacervation, occurs within living cells to form "membraneless organelles": biomolecule-dense droplets that affect cellular biochemistry (1), including within the nucleus (2). The spatially and physically distinct spaces created by LLPS-based compartmentalization, and the ability to replicate the process outside of living cells, make it an intensively studied synthetic biology system (3–5). For the same reasons, LLPS has long attracted interest as a potential compartmentalization mechanism in origin-of-life research (6). Finally, LLPS is also of technological interest, as the resulting droplets are capable of encapsulating and/or delivering pharmaceutically active drugs or enzymes (7).

The functions of macromolecular LLPS droplets are dependent on the complex interactions of the liquid "scaffold" with solutes ("clients"), including enzymes (8, 9). For example, the function of the LLPS-based nucleolus depends on the localization and activity of the enzyme RNA polymerase (8, 10). Further, interactions of droplets with enzymatic solutes has been shown to enable triggered droplet condensation or dissolution (11, 12), cargo release (12), ribozyme activity (13), transcription (14, 15), and droplet shape changes (16).

While the coacervate droplet/enzymatic solute interaction is of broad importance, there are relatively few quantitative physical studies of the microscopic mechanisms that govern this interaction. To remedy this, we have developed a model system of the interaction that permits high-resolution measurement and physical interpretation, consisting of a liquid-forming system of DNA that is acted upon, and degraded by, a DNA-cleaving restriction enzyme.

The liquid is formed from self-assembled DNA particles. A DNA-based liquid system has strengths as a model system, owing to the ability to exploit sequence design to control particle shape, enzyme interactions, and interparticle binding. As shown by Seeman and coworkers (17, 18), condensed DNA phases can be formed by base-pairing interactions between multivalent structures; this has been used to create static gels (19, 20) that have been interfaced with enzymes (21–23). Here, we focus on a liquid-forming multivalent particle termed the DNA nanostar (24). A DNA nanostar consists of multiple double-stranded DNA arms emanating from a common three- or four-way junction, with each arm terminating in a single-stranded region (a sticky end). Hybridization of sticky ends causes nanostars to bind each other, driving phase separation (24) and the formation of viscoelastic liquids, whose behavior can be controlled through sequence design (25–28). DNA nanostars condense into a liquid, rather than a crystalline solid or kinetically arrested gel, due to the reduced particle valence (24, 29), the labile sticky ends, and the internal particle flexibility induced by the presence of unpaired bases at the junction and near the sticky end (30, 31).

We design restriction-enzyme cleavage sites into the arms of DNA nanostars and induce phase separation, creating

Significance

Biomolecules, such as proteins or nucleic acids, can condense into liquid droplets whose biological or technological function depends on interactions with other solutes. We explore such interactions using a system of self-assembled DNA particles that forms liquid droplets which are degraded by an active solute, a restriction enzyme. We find that enzymes are able to penetrate the droplets when the liquid is poised near the phase boundary, enhancing the degradation rate and, in certain cases, causing internal bubbling. These results point to a complex interplay of phase stability and solute transport in liquid–liquid phase-separating macromolecular systems.

Author contributions: O.A.S. and T.L. designed research; O.A.S. performed research; B.J. contributed new reagents/analytic tools; O.A.S. analyzed data; O.A.S. and T.L. wrote the paper; and B.J. commented on the paper.

The authors declare no competing interest.

This article is a PNAS Direct Submission.

Published under the PNAS license.

Data deposition: Raw data of droplet-radius trajectories, example image analysis code, and code underlying the diffusion analysis have been deposited in the Dryad Digital Repository (https://doi.org/10.25349/D95G66).

[1]To whom correspondence may be addressed. Email: saleh@ucsb.edu.

This article contains supporting information online at https://www.pnas.org/lookup/suppl/doi:10.1073/pnas.2001654117/-/DCSupplemental.

First published June 29, 2020.

micrometer-scale spherical droplets of DNA. Addition of the restriction enzyme causes the droplets to shrink as cleavage events remove DNA fragments from the dense liquid phase. We find that the degradation rate strongly changes as a function of the collective stability of the liquid phase: A scaling analysis indicates that nanostar liquids that are farther from the phase boundary (i.e., farther from the dissolution, or boiling, temperature, T_b) are degraded only on the droplet surface, while those poised near the boundary permit enzyme penetration. We suggest that proximity to the phase boundary accelerates liquid dynamics, thus enhancing the diffusive transport and internalization of the enzymes. This is corroborated by the observation of enzyme-induced bubbling events within nanostar liquid droplets that are relatively close to T_b.

Results and Discussion

DNA Nanostar Structure. DNA nanostars were designed following the work of Biffi et al. (24), in which each nanostar has three or four double-stranded DNA arms joined at a junction by flexible, unpaired bases (Fig. 1). Distal to the junction, each arm terminates in a six-base sticky-end sequence; this sequence is palindromic, permitting two identical nanostars to bind. We used the NUPACK DNA design software (32) to create specific sequence designs for DNA oligomers that assemble into three- or four-armed nanostars. Oligomer sequences are given in *SI Appendix*, Table S1.

All nanostars also contained a six-base restriction enzyme-cleavage site, with sequence *CCCGGG*, in the center of all but one of their arms (Fig. 1). This sequence is recognized and cleaved by the type-2 restriction endonuclease SmaI. We chose the enzyme SmaI for two reasons: First, SmaI cleavage results in blunt-ended fragments rather than the four-base sticky ends common to other restriction enzymes; this minimizes the chance of fragment rebinding after cleavage. Second, SmaI retains strong cleavage activity at room temperature, simplifying our imaging-based experimental protocols.

Experiments were carried out by using nanostars with different sequences of the palindromic sticky end (Fig. 2). The binding strength for each sticky end can be estimated by using the melting temperature, T_m, predicted for the specific sequence by validated software models [DinaMelt (33)], in the relevant ionic strength and using a reasonable oligo concentration (40 μM, corresponding to 4× the typical nanostar concentration). We designed two types of four-armed nanostars, both using 5′ sticky-end extensions: "Weak tetramers" utilized the binding sequence *CGATCG*, with $T_m \approx 27.8$ °C, while "strong tetramers" utilized the binding sequence *ACCGGT*, with $T_m \approx 32.7$ °C). We used one type of three-armed nanostar ("trimer") that had a 3′ extension with binding sequence *TGGCCA* ($T_m \approx 33.3$ °C). Note that T_m for the trimer and strong tetramer are nearly identical.

These T_m estimates are a simple benchmark for binding strength that ignores both the effects of flanking bases and the effects that drive phase separation, such as the total number of sticky-end bonds per nanostar, and the change in nanostar entropy between dense and dilute phases (34). Single-overhang melting points are thus indicative only of local bond stability; the stability of the entire liquid is better measured by the phase transition point, i.e., the dissolution temperature T_b, which is sensitive to both bond strength and particle valence (34). By visualizing the appearance of droplets of nanostar liquid with varying temperature (*SI Appendix*, Fig. S2), we experimentally estimated T_b for each design, finding the strong tetramer to have $T_b \approx 32$ °C, the weak tetramer to have $T_b \approx 28$ °C, and the trimer to have $T_b \approx 29$ °C. While the trimer and strong-tetramer nanostars have near-identical single-bond T_m values, the difference in valence leads to an appreciable difference in T_b.

Droplet Formation, Adhesion, and Introduction of Enzyme. Sample preparation was carried out as depicted in Fig. 1; details are provided in *Materials and Methods*. Briefly, DNA nanostars were assembled by mixing equal amounts of the component oligonucleotides, including a small fraction labeled with a fluorescent dye, in a 10 mM ionic-strength buffer that does not favor sticky-end binding. To anneal the nanostars, the mixture was heated to 95°C and cooled to room temperature over 2 h. Then, salt was added, activating nanostar–nanostar binding and condensing liquid droplets. The final salt conditions were chosen to optimize later enzymatic activity. The solution was continuously rotated for 1 h to allow droplet growth without sedimentation. The resulting solution was then added to a flow cell consisting of a glass coverslip with a hydrophobic coating and channels that permit fluid exchange. Droplets sedimented onto the

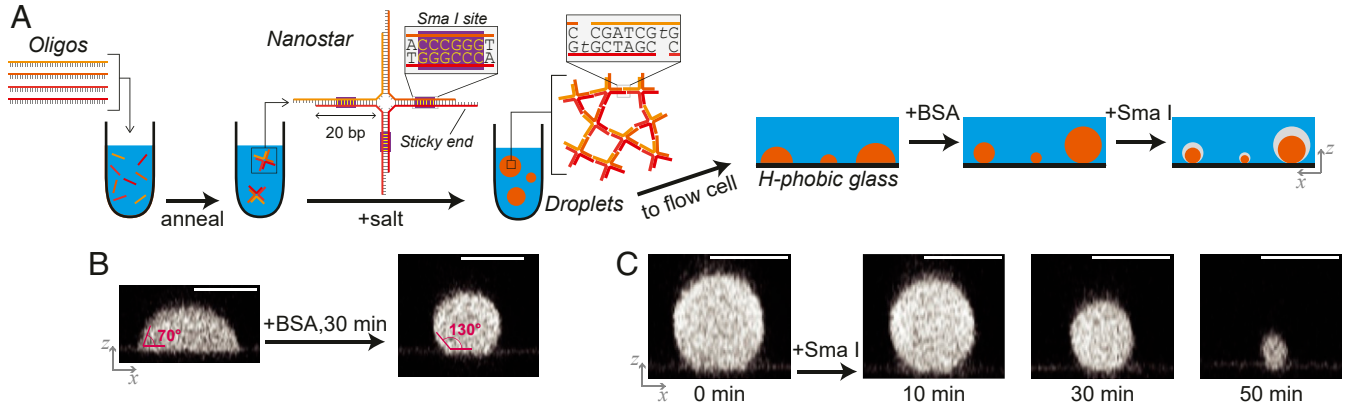

Fig. 1. (*A*) Schematic of experimental protocol: Single-stranded DNA oligomers are annealed to form DNA nanostar particles, whose arms contain recognition sequences, *CCCGGG*, for the restriction enzyme SmaI. Addition of salt condenses nanostars into liquid droplets due to base pairing between nanostar sticky ends. The binding schematic depicts the sequence of "weak tetramer" nanostars (Fig. 2*A*), with lowercase letters indicating bases left unpaired in the bound state. Droplets are added to a flow cell, where they adhere to a hydrophobic glass surface. Addition of BSA causes partial dewetting, creating lightly adhered, near-spherical DNA droplets that degrade with time upon SmaI addition. (*B*) Confocal (*x*, *z*) image slice through the center of a fluorescently labeled DNA droplet, before and after BSA addition, demonstrating dewetting. Approximate contact angles are noted. See also *SI Appendix*, Movie S1. (Scale bars: 20 μm.) (*C*) Time course of enzymatic degradation of a single droplet visualized by using confocal (*x*, *z*) slices. The droplet shrinks while retaining a constant contact angle and a near-spherical lateral profile. (Scale bars: 20 μm.) Droplets in *B* and *C* are formed from weak tetramer nanostars.

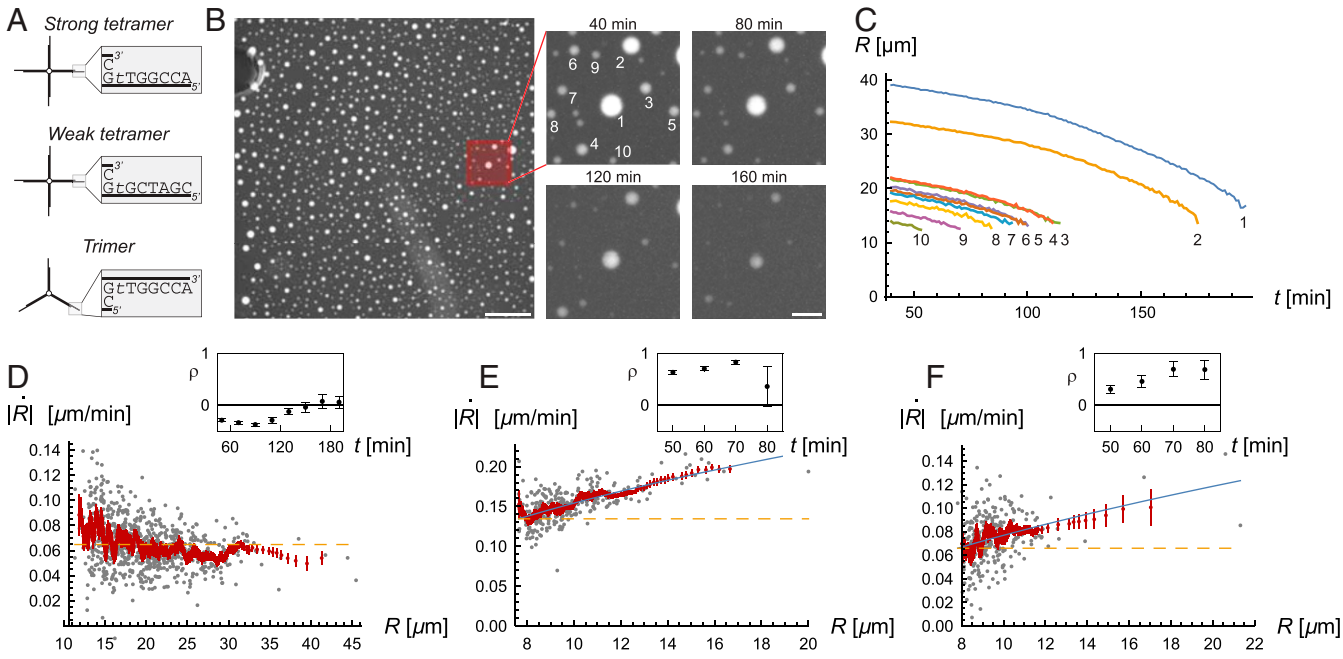

Fig. 2. (*A*) Schematic of three nanostar designs, with sticky-end sequences. Lowercase letters indicate bases left unpaired after nanostar–nanostar binding. (*B*, *Left*) Low-magnification epifluorescent micrograph of fluorescently labeled strong tetramer droplets, 40 min after SmaI addition. Approximately 900 droplets are visible. (Scale bar: 500 μm.) (*B*, *Right*) Small micrographs show the time course of images of 10 selected droplets as they are degraded by the enzyme. (Scale bar: 100 μm.) (*C*) Radius, *R*, vs. time, *t*, for the 10 selected droplets from *B*. (*D*–*F*) Degradation rate, $|\dot{R}|$, vs. radius, *R*, 50 min after enzyme addition, for 808 droplets of strong tetramer nanostars, from the experiment shown in *B* and *C* (*D*); 298 droplets of weak tetramer nanostars (*E*); and 295 droplets of trimer nanostars (*F*). Dark gray points depict individual droplets, while red points indicate a moving average of $|\dot{R}|$ using a window size of 19 points (error bars: SEM), with the window size tapering to five points at the extrema. Blue lines in *E* and *F* are power laws, $|\dot{R}| \sim R^p$, fitted to individual droplet points, with best-fit exponents of, respectively, $p = 0.51 \pm 0.04$ and $p = 0.62 \pm 0.1$. Yellow dashed lines are guides to the eye, indicating a constant $|\dot{R}|$ aligned in *D* to the mean of all points, and in *E* and *F* to the rate at small *R*. (*D*–*F*) The *Insets* show the correlation between $|\dot{R}|$ and *R* as the Pearson's coefficient, ρ, plotted vs. time since enzyme addition, for all time points with at least 10 droplets remaining (error bars are from bootstrapping). All data were acquired at $T = 26$ °C.

hydrophobic surface and adhered, displaying a contact angle of $\approx 70^\circ$ (Fig. 1*B*). We attribute this to the affinity of the single-stranded sticky ends for hydrophobic surfaces; indeed, we found that droplets do not adhere to hydrophilic (clean glass) surfaces (*SI Appendix*, Fig. S3).

Quantification of degradation was simplified when the droplets form nearly complete spheres whose size is encoded in their radius, R, rather than the flat, irregular wetting structures that resulted from strong surface adhesion. We found that, after initial adhesion, addition of 0.1 mg/mL bovine serum albumin (BSA) caused the droplets to partially de-adhere (contact angles grew to $\gtrsim 130^\circ$; Fig. 1*B*), forming near-complete spheres (Fig. 1 and *SI Appendix*, Movie S1). A 30-min BSA incubation was a good compromise: Droplets were induced to form spheres, but remained lightly adhered, and thus could withstand additional fluid handling without washing away. Over long times (multiple hours), droplets would sometimes de-adhere, as evidenced by the onset of lateral motion; in our measurements, we stopped quantifying droplet behavior if this was detected.

Once lightly adhered droplets were formed and equilibrated at $T = 26$ °C, we added the restriction enzyme, SmaI, to a concentration of 3 nM. The resulting degradation was quantified by time-lapse fluorescent imaging of the droplets. Confocal imaging enabled three-dimensional characterization of droplet shape during degradation, and demonstrated that the droplets were nearly spherical while shrinking, without contact-line pinning (Fig. 1*C*).

Wide-Field Imaging. While the images depicted in Fig. 1 are important to validate adhesion mechanisms and droplet morphology, in practice, the confocal approach had poor data throughput due to limitations of the imaging speed and the field of view. To enhance data throughput, we visualized droplet degradation with an epifluorescent microscope and using a low-magnification objective. This provided both a wide field of view (allowing simultaneous measurement of many droplets) and a deep focal field (thus capturing all droplet fluorescence in the image, allowing high-resolution estimate of R; *SI Appendix*, Fig. S4) (35). These experiments resulted in multihour videos of a few hundred droplets imaged at 1-min intervals; a typical frame is shown in Fig. 2*B*.

Wide-field fluorescent movies were analyzed to estimate the radius trajectory, $R(t)$, of each visualized droplet, and thus to quantify the response to added restriction enzyme. Typical trajectories after enzyme addition are shown in Fig. 2*C*. The trajectories indicate that R decreases monotonically with t, eventually leading to complete droplet disappearance, due to the cleavage activity of SmaI. Control experiments confirmed the specific role of SmaI cleavage: Injecting an enzyme-free aliquot, or one containing a different restriction enzyme, caused no significant changes in droplet size (*SI Appendix*, Figs. S5 and S6).

Scaling Analysis. Historically, analysis of the deterioration of solid or liquid particles has focused on the scaling with R of the volume rate of degradation, $|dV/dt| \equiv |\dot{V}|$. For example, for a droplet evaporating into gas, Maxwell predicted degradation to be limited by diffusion in the gas phase, leading to $|\dot{V}| \sim R$ (36). For the case of dissolution of a solid particle into solvent, work by Noyes, Whitney, Nernst, and others (37) indicated $|\dot{V}| \sim R^2$,

which corresponds to the rate being limited by transport through the particle surface. By extension, if the rate-limiting step of degradation is a process that occurs uniformly throughout the droplet, we expect $|\dot{V}| \sim R^3$, i.e., a sensitivity to droplet volume.

These considerations show that mechanistic details of nanostar droplet degradation by SmaI can be inferred by measuring the relation of degradation rate to droplet size. Such a scaling analysis benefits from being simple and robust. We focus on the relation of the radius rate of degradation to radius, $|\dot{R}| \sim R^p$. Since $|\dot{R}| \sim |\dot{V}|/R^2$, an area-controlled process has no dependence of $|\dot{R}|$ on R (i.e., $p = 0$), while a volume-controlled process has $p = 1$, and $|\dot{R}|$ increases with R.

Our scaling analysis of $|\dot{R}|$ vs. R for strong tetramer nanostars droplets degraded by SmaI indicates that surface area controls dissolution of these droplets, as there is no dependence of $|\dot{R}|$ on R (Fig. 2*D*). This can be seen by calculating the Pearson correlation coefficient, ρ, between $|\dot{R}|$ and R; note that $\rho = \pm 1$ would occur if the two datasets were perfectly correlated/anticorrelated, while $\rho = 0$ would occur if the two datasets were mutually random. For the strong tetramers, we found that ρ was small, increasing from ≈ -0.3 to ≈ 0.1 over the course of a multihour experiment (Fig. 2 *D*, *Inset*). The invariance of $|\dot{R}|$ with R persisted at all time points (Fig. 2 *D*, *Inset* and *SI Appendix*, Figs. S7 and S8).

Penetration of the enzyme through the nanostar liquid is possible on geometric grounds; that it does not happen for the strong tetramer liquid is likely due to relatively fast cleavage rates relative to transport timescales. Solute penetration through a network is possible when its diameter is less than the network mesh size (38). Here, that condition is met, as the SmaI diameter, as estimated from the molecular weight (39), is 5.1 nm, compared to the mesh size of the nanostar liquid of about 9 nm (40). However, binding of the enzyme to network strands will retard transport (41). A lower bound for the rate of this process can be estimated by assuming that SmaI penetrates a static meshwork by hopping between strands with each hop traveling a few mesh sizes, and with a time between hops of around 1 s based on measurements of SmaI kinetics (42) Using these parameters in a random-walk model (43) gives a diffusion coefficient of $D_{hop} \approx 9 \times 10^{-4}$ μm^2/s, and thus a $\approx$20-h timescale to diffuse to the center of an $R = 20$ μm droplet. Our data show that such a droplet is instead completely degraded on a much faster time scale, $\lesssim$2 h (Fig. 2*C*). Such degradation rates are consistent with expectations for a surface-dominated process: At maximal speed, the SmaI cleavage rate is 0.3/s (42); if this is the rate-determining step, each cleavage event removes a single nanostar arm of 8 nm, SmaI covers the droplet surface, and the expected droplet degradation rate is $|\dot{R}| \approx 2$ nm/s $\approx$ 0.1 μm/min, in good agreement with the data (Fig. 2*D*). In reality, the nanostar liquid is dynamic, which can increase D over D_{hop} (see below) (41); nonetheless, these considerations indicate that surface-controlled degradation of strong tetramer droplets is a consequence of cleavage outpacing binding-retarded diffusive transport.

Controlling Enzyme Penetration. Measurements of the degradation of weak tetramer droplets differed from those on the strong tetramer droplets, indicating differences in the ability of the enzyme to penetrate the two liquids. The degradation rate, $|\dot{R}|$, of weak tetramer droplets increased with R, with correlation $\rho \approx$ 0.6 to 0.8 (Fig. 2*E*). Power-law fits indicate an exponent $p \approx 0.5$ at early times (Fig. 2*E*), which grows to $p \approx 0.9$ at later times (*SI Appendix*, Figs. S7 and S8). These values lie between the surface-controlled ($p = 0$) and volume-controlled ($p = 1$) limits. Thus, the scaling analysis indicates partial penetration of the enzyme into the weak tetramer droplets.

The scaling picture is corroborated by a model of the diffusive behavior of a solute, at constant bulk concentration c_0, as it penetrates an initially solute-free sphere, as controlled by the solute diffusion constant D within the sphere (Fig. 3 and *SI Appendix*, section S1) (35). The solution to the diffusion equation in a spherical geometry gives the time course of the solute's radial concentration, $c(r, t)$, as controlled by the characteristic time $\tau \equiv R^2/\pi^2 D$ (Fig. 3*A*) (44). We assume that the degradation rate depends on the amount of solute within the sphere. Thus, integrating the $c(r, t)$ curves enables prediction of the time dependence of p, which transitions from zero (surface-controlled) to one (volume-controlled) as t increases through τ (Fig. 3*B*). For $t \approx \tau$, the values of p are similar to those in the weak tetramer experiment (Fig. 2 and *SI Appendix*, Figs. S7 and S8). We use the prediction to extract values of τ from measured exponents (gray lines, Fig. 3*B*), which, along with the known R, allows estimation of D (Fig. 3*C*); we consistently find $D \approx 15 \times 10^{-3}$ μm^2/s for both trimer and weak-tetramer liquids at various time points. This value is much larger than D_{hop} and much smaller than the expected free solution value ($D \approx 100$ μm^2/s). It is similar to that measured for diffusion of weak tetramer nanostars within a nanostar liquid in comparable conditions ($D_{ns} \approx 4 \times 10^{-3}$ μm^2/s) (27), implying that the enzyme penetrates the liquid by binding to, and diffusing together with, the liquid's constituent particles.

The weak- and strong-tetramer nanostar liquids differ both in sticky-end stability (T_m) and bulk stability (T_b). To isolate which material parameter leads to the different enzyme behaviors, we measured degradation of the trimers, which have near identical T_m to the strong tetramers, but similar T_b to the weak tetramers. The trimer degradation data at 26 °C (Fig. 2*F* and *SI Appendix*, Figs. S7 and S8) is similar to the weak tetramer degradation: $|\dot{R}|$ increases with R ($\rho \approx 0.3 - 0.7$),

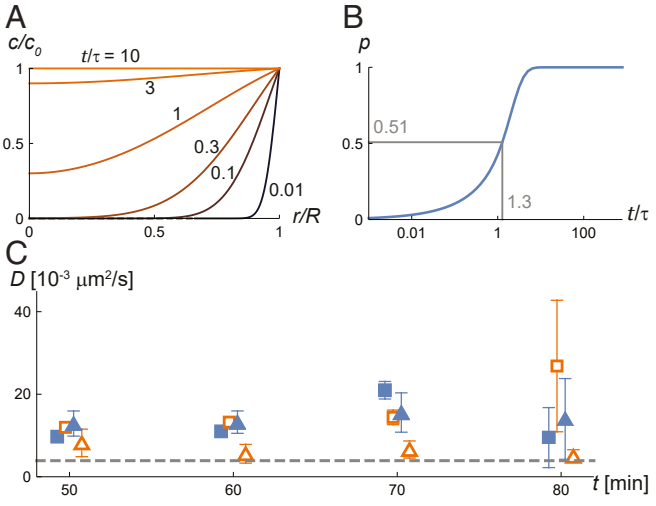

Fig. 3. Results of a diffusion model of enzyme penetration of spherical droplets (*SI Appendix*, section S1) (35). (*A*) Relative radial solute concentration, $c(t, r)/c_0$, vs. relative radius, r/R, at various time points, as labeled; note $\tau = R^2/\pi^2 D$. (*B*) Predicted degradation exponent p vs. t/τ. Gray lines show one example (of eight) of the interpolation procedure that estimates t/τ from a measurement of p (here, using values from Fig. 2*E*). (*C*) Diffusion coefficients, D, estimated from measurements of p, for SmaI within nanostar droplets at various time points. Squares, weak tetramers; triangles, trimers; filled symbols, data from Fig. 2 and *SI Appendix*, Fig. S7; open symbols, data from *SI Appendix*, Fig. S8. Points shifted slightly in t for clarity. The dashed line indicates the nanostar diffusion constant, D_{ns}, as measured from weak tetramer droplets in comparable conditions (27). Error bars originate from the fit error in p, and increase with t as the number of remaining droplets decreases (*SI Appendix*, Figs. S7 and S8).

indicating significant enzyme penetration. The measured degradation exponents, $p \approx 0.4 - 0.8$, are again consistent with $D \approx 15 \times 10^{-3}$ μm^2/s (Fig. 3). The values of ρ and p from the trimers indicate that proximity to the boiling point, and not the stability of single bonds, controls penetration of the enzyme into the liquid. This finding was supported by a control experiment using the weak tetramers, but carrying out the experiment at 22 °C, i.e., roughly 6 °C below T_b. In that condition, $|\dot{R}|$ vs. R curves were constant (uncorrelated), indicating a lack of penetration (*SI Appendix*, Fig. S9). While altering the temperature can affect many biomolecular parameters (such as enzymatic rates or binding affinities), the different scaling for the weak tetramers at 22 °C relative to that at 26 °C confirms a temperature dependence of enzyme penetration. Those results, in combination with the results from the trimers at 26 °C, indicate that it is temperature relative to T_b, and not T_m, that controls enzyme penetration.

Bubbling. Another observation supports our conclusion that enzyme penetration is indeed the mechanism underlying the $|\dot{R}|$ vs. R behavior: In experiments carried out at 26°C, several of the largest weak-tetramer and trimer droplets showed internal vacuole formation (Fig. 4 and *SI Appendix*, Movie S2). In particular, across six experiments, there were 27 trimer and weak-tetramer droplets larger than 25 μm at $t = 50$ min; of these, vacuoles appeared in 13 droplets. Vacuoles typically appeared at $t = 60$ to 80 min, though in a few cases did not appear before $t = 120$ min. The vacuoles were frequently dynamic, going through cycles of growth, popping, and regrowth (*SI Appendix*, Movie S2). Just before popping, the vacuoles expanded the affected droplet beyond its original dimensions, indicating that the vacuoles were swollen by an internal pressure. Vacuole formation was never observed in the strong-tetramer droplets.

We attribute vacuole formation to a cluster of colocalized enzymes deep within a droplet, occurring either through random transport processes, or perhaps a discrete instability event in the liquid (Fig. 4*C*). DNA cleavage by such internalized enzymes could generate DNA fragments more rapidly than the fragments can escape from the droplet, due to the throttling effect on fragment transport of the intervening nanostar meshwork; throttling is likely since the fragments are not much smaller than the 9-nm mesh size (38, 40). Indeed, transport of fragments through the meshwork will be particularly slow, and thus internal build-up of fragment concentration most likely, within thick shells of nanostar liquid, potentially explaining why vacuoles only appear in the largest droplets. The mesh size is large relative to water, so should always allow rapid water transport; thus, the entrapped fragments will create an osmotic pressure, leading to swelling. Consequently, the vacuole grows as more fragments are generated, eventually expanding to reach the droplet surface, at which point the internal fragments are released, the osmotic pressure decreases, and the vacuole shrinks; however, the enzyme is still entrapped, likely through binding to uncut nanostars at the vacuole/droplet interface, and the cycle starts again.

Prior work has observed vacuole formation within biomolecular liquid droplets, both in vivo (45) and in vitro (46). In those systems, vacuole formation was preceded by a change to conditions in which the dense liquid phase was no longer stable with respect to the dilute solution. Vacuole appearance was then attributed to nucleation and growth of the stable dilute phase within the metastable dense liquid, a thermally activated phase-transformation process. In contrast, here, the liquid is stable with respect to phase change, but is nonetheless transformed by an process that is active and nonthermal: enzymatic cleavage of the DNA backbone.

Conclusion

Our results show that a liquid DNA phase is degraded by an active solute, a restriction enzyme, in a manner dependent on the proximity of the liquid phase to its phase-transition (boiling) point. Far from this point (i.e., when $T_b - T > 3$ °C), liquid droplets form a relatively stable meshwork to which the enzymes bind, hindering their transport, and allowing cleavage to occur before the enzyme significantly penetrates the liquid. As a consequence, the degradation-driven inward velocity of the surface outpaces the rate of enzyme transport, and the enzymes are effectively only active on the surface. This leads to the measured scaling of droplet degradation rate with surface area, $\dot{V} \sim R^2$ and, equivalently, $|\dot{R}| \sim R^0$.

In contrast, liquid droplets poised closer to the boiling point ($T_b - T \approx 3$ °C) show two experimental signatures of significant enzyme penetration: a positive correlation of degradation

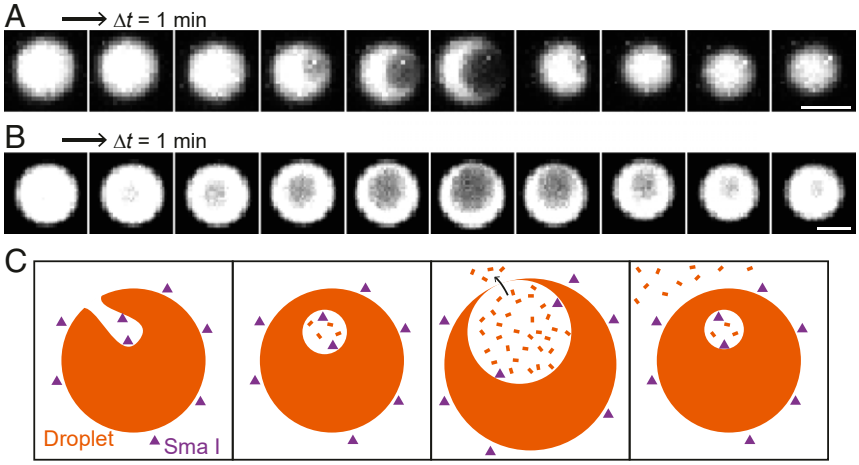

Fig. 4. (*A* and *B*) Time series of images, on a 1-min interval, showing vacuole appearance, growth, and popping in large droplets of weak tetramers (*A*) and trimers (*B*). Vacuoles appear repeatedly in these droplets, giving the appearance of bubbling (*SI Appendix*, Movie S2). (Scale bars: 20 μm.) (*C*) Schematic of suggested mechanism of enzyme-induced bubbling. A cluster of SmaI (purple triangles) penetrates deep into a liquid DNA droplet (orange), perhaps through a dynamic instability, as shown. Enzymatic activity quickly generates restriction fragments (orange lines), causing an osmotic pressure that creates and swells the vacuole. The vacuole grows until it reaches the droplet surface, where the pressure is released by fragment outflow, causing the vacuole to shrink. The enzymes remain internalized and catalyze a new vacuole growth cycle.

rate with droplet size, and the appearance of vacuoles. This indicates that, in these systems, the liquid meshwork allows the solutes to quickly move through the droplet and become internalized at speeds that exceed the degradation rate. The diffusion analysis shows a quantitative similarity between enzyme transport and that of the nanostars themselves, as measured in prior work (27); this argues for a "piggy-back" mechanism, in which enzyme motion is dictated by the dynamics of the nanostars to which they are bound. This underlying liquid dynamics is arrested for $T \ll T_b$ (47), consistent with the slower dynamics observed in strong tetramer droplets. That said, other mechanisms could play a role as T approaches T_b: For example, it is possible that critical fluctuations create dynamic voids through which enzymes can quickly diffuse; alternatively, closer to the boiling point, nanostar bond strength will be reduced, which could accelerate transport by increasing the mesh size.

Generally, the results presented here demonstrate a mechanism through which the phase stability of a liquid controls its own enzymatic degradation through modulation of enzyme transport properties. We expect that these results will inform understanding of biological LLPS phenomena, which frequently depend on the activity and transport of client solutes within a host droplet (8, 9), as well as design of biomolecular liquids in synthetic biology and biotechnological applications.

Materials and Methods

Experimental Setup. Nanostars were formed by mixing a concentration of 10 μM of each component oligomer, plus a concentration of 0.1 μM of one of the oligomers carrying a 5′ Cy3 fluorophore label, in a solution containing 4 mM Tris buffer and 10 mM K–acetate, pH 7.9. DNA sequences are given in *SI Appendix*, Table S1. This solution was placed in a thermocycler, held at 95°C for 2 min, and then cooled to room temperature over 2 h. The solution was adjusted to concentrations of 20 mM Tris, 50 mM K–acetate and 10 mM Mg–acetate, pH 7.9, then placed on a rotator for 1 h at room temperature to allow droplet growth without sedimentation. The droplet solution was then added to a pre-wet flow cell consisting of a clean glass coverslip coated in the hydrophobic silane SigmaCote (Sigma), with channels formed by using a commercial multichannel device (sticky-Slide VI, Ibidi). Droplets were allowed to sediment and adhere for 45 min, and then the channel was flushed with a solution with identical salt and buffer concentrations, but now containing 0.1 mg/mL BSA, and the system was placed on the microscope stage, held at the desired experimental temperature, and incubated for 30 min. A small aliquot of SmaI (New England Biolabs) was then added to a concentration of 3 nM, and the solution in the channel was gently mixed by repetitively transferring small volumes of liquid between the two reservoirs at each end of the channel. Mineral oil was layered on top of each reservoir to stop evaporation, and then imaging was started.

Imaging. Wide-field, epifluorescent measurements used a Nikon Eclipse Ti Microscope outfitted with an Okolab Cage Incubator, a Lumencor Sola solid-state white-light excitation source, and a Chroma DSRed ET filter cube, with images captured by a 4× objective and a pco.edge scientific complementary metal oxide semiconductor camera. Confocal measurements used a Carl Zeiss ConfoCor2 laser-scanning module, an Axiovert200 microscope, and a 40× water-immersion objective, with excitation by a 543-nm HeNe laser and emission captured through a 560-nm long-pass filter. In all setups, illumination levels were optimized so as to avoid photodamage and photobleaching while permitting sufficient signal with respect to the optical noise arising from photon-shot noise and pixel noise in the camera.

Image Analysis. To find droplet radii, each image frame was binarized by using a threshold set to 1.5× the mean background intensity, and droplet locations, circularity, and approximate sizes were found using the *ComponentMeasurements* function in Mathematica (Wolfram Research). These initial measurements were used to reject noncircular droplets, or those that were too small. The remaining droplets were analyzed with a precise radius-measurement scheme, which fit the droplet intensity profile to that expected for a sphere projected into the two-dimensional image plane (*SI Appendix*, Fig. S4) (35). The resulting $R(t)$ data were then either plotted or smoothed with a moving average filter (20-point window) to calculate $\dot{R}$.

Data Availability. Raw data of droplet-radius trajectories, example image analysis code, and code underlying the diffusion analysis have been deposited in the Dryad Digital Repository, available at https://doi.org/10.25349/D95G66.

ACKNOWLEDGMENTS. This work was primarily supported by Deutsche Forschungsgemeinschaft Grant SFB1032 (Project A6). O.A.S. was supported by the Alexander von Humboldt Foundation. Aspects of the adhesion protocol were developed with support from the U.S. Department of Energy, Office of Science, Basic Energy Sciences Award DESC0014427. We thank Joachim Raedler for use of the fluorescent microscopes.

1. A. A. Hyman, C. A. Weber, F. Jülicher, Liquid-liquid phase separation in biology. *Annu. Rev. Cell Dev. Biol.* **30**, 39–58 (2014).
2. I. A. Sawyer, D. Sturgill, M. Dundr, Membraneless nuclear organelles and the search for phases within phases. *Wiley Interdiscip Rev. RNA* **10**, e1514 (2019).
3. C. D. Crowe, C. D. Keating, Liquid–liquid phase separation in artificial cells. *Interface Focus* **8**, 20180032 (2018).
4. N. Martin, Dynamic synthetic cells based on liquid–liquid phase separation. *Chembiochem* **20**, 2553–2568 (2019).
5. M. Li, X. Huang, T. Y. Tang, S. Mann, Synthetic cellularity based on non-lipid microcompartments and protocell models. *Curr. Opin. Chem. Biol.* **22**, 1–11 (2014).
6. A. Oparin, *The Origin of Life* (MacMillan, New York, NY, 1938).
7. W. C. Blocher, S. L. Perry, Complex coacervate-based materials for biomedicine. *Wiley Interdiscip. Rev. Nanomed. Nanobiotechnol.* **9**, e1442 (2017).
8. J. A. Ditlev, L. B. Case, M. K. Rosen, Who's in and who's out—compositional control of biomolecular condensates. *J. Mol. Biol.* **430**, 4666–4684 (2018).
9. K. K. Nakashima, M. A. Vibhute, E. Spruijt, Biomolecular chemistry in liquid phase separated compartments. *Front. Mol. Biosci* **6**, 21–21 (2019).
10. M. Feric *et al.*, Coexisting liquid phases underlie nucleolar subcompartments. *Cell* **165**, 1686–1697 (2016).
11. K. K. Nakashima, J. F. Baaij, E. Spruijt, Reversible generation of coacervate droplets in an enzymatic network. *Soft Matter* **14**, 361–367 (2018).
12. B. S. Schuster *et al.*, Controllable protein phase separation and modular recruitment to form responsive membraneless organelles. *Nat. Commun.* **9**, 2985 (2018).
13. R. R. Poudyal *et al.*, Template-directed RNA polymerization and enhanced ribozyme catalysis inside membraneless compartments formed by coacervates. *Nat. Commun.* **10**, 490 (2019).
14. T. Y. D. Tang, D. van Swaay, J. R. Anderson, S. Mann, In vitro gene expression within membrane-free coacervate protocells. *Chem. Commun.* **51**, 11429–11432 (2015).
15. E. Sokolova *et al.*, Enhanced transcription rates in membrane-free protocells formed by coacervation of cell lysate. *Proc. Natl. Acad. Sci. U.S.A.* **110**, 11692–11697 (2013).
16. W. K. Spoelstra, E. O. van der Sluis, M. Dogterom, L. Reese, Nonspherical coacervate shapes in an enzyme-driven active system. *Langmuir* **36**, 1956–1964 (2020).
17. NC. Seeman, Nucleic acid junctions and lattices. *J. Theor. Biol.* **99**, 237–247 (1982).
18. E. Winfree, F. Liu, L. A. Wenzler, NC. Seeman, Design and self-assembly of two-dimensional DNA crystals. *Nature* **394**, 539–544 (1998).
19. Y. Li *et al.*, Controlled assembly of dendrimer-like DNA. *Nat. Mater.* **3**, 38–42 (2003).
20. E. Cheng *et al.*, A pH-triggered, fast-responding DNA hydrogel. *Angew. Chem. Int. Ed.* **48**, 7660–7663 (2009).
21. S. H. Um *et al.*, Enzyme-catalysed assembly of DNA hydrogel. *Nat. Mater.* **5**, 797–801 (2006).
22. J. B. Lee *et al.*, A mechanical metamaterial made from a DNA hydrogel. *Nat. Nanotechnol.* **7**, 816–820 (2012).
23. O. J. N. Bertrand, D. K. Fygenson, O. A. Saleh, Active, motor-driven mechanics in a DNA gel. *Proc. Natl. Acad. Sci. U.S.A.* **109**, 17342–17347 (2012).
24. S. Biffi *et al.*, Phase behavior and critical activated dynamics of limited-valence DNA nanostars. *Proc. Natl. Acad. Sci. U.S.A.* **110**, 15633–15637 (2013).
25. N. Conrad, T. Kennedy, D. K. Fygenson, O. A. Saleh, Increasing valence pushes DNA nanostar networks to the isostatic point. *Proc. Natl. Acad. Sci. U.S.A.* **116**, 7238–7243 (2019).
26. Y. Sato, T. Sakamoto, M. Takinoue, Sequence-based engineering of dynamic functions of micrometer-sized DNA droplets. *Sci. Adv.* **6**, eaba3471 (2020).
27. Bj. Jeon *et al.*, Salt-dependent properties of a coacervate-like, self-assembled DNA liquid. *Soft Matter* **14**, 7009–7015 (2018).
28. Z. Xing *et al.*, Microrheology of DNA hydrogels. *Proc. Natl. Acad. Sci. U.S.A.* **115**, 8137–8142 (2018).
29. E. Bianchi, J. Largo, P. Tartaglia, E. Zaccarelli, F. Sciortino, Phase diagram of patchy colloids: Towards empty liquids. *Phys. Rev. Lett.* **97**, 168301 (2006).
30. L. Rovigatti, F. Smallenburg, F. Romano, F. Sciortino, Gels of DNA nanostars never crystallize. *ACS Nano* **8**, 3567–3574 (2014).
31. D. T. Nguyen, O. A. Saleh, Tuning phase and aging of DNA hydrogels through molecular design. *Soft Matter* **13**, 5421–5427 (2017).
32. J. N. Zadeh *et al.*, Nupack: Analysis and design of nucleic acid systems. *J. Comput. Chem.* **32**, 170–173 (2011).
33. N. R. Markham, M. Zuker, Dinamelt web server for nucleic acid melting prediction. *Nucleic Acids Res.* **33**, W577–W581 (2005).

34. L. Rovigatti, F. Bomboi, F. Sciortino, Accurate phase diagram of tetravalent DNA nanostars. *J. Chem. Phys.* **140**, 154903 (2014).
35. O. A. Saleh, Data from: Enzymatic degradation of liquid droplets of DNA is modulated near the phase boundary. Dryad Digital Repository. https://doi.org/10.25349/D95G66. Deposited 5 May 5 2020.
36. J. C. Maxwell, *The Scientific Papers of James Clerk Maxwell* (Cambridge University Press, Cambridge, UK, 1890), vol. 2.
37. A. Dokoumetzidis, P. Macheras, A century of dissolution research: From Noyes and Whitney to the biopharmaceutics classification system. *Int. J. Pharm.* **321**, 1–11 (2006).
38. S. R. Lustig, N. A. Peppas, Solute diffusion in swollen membranes. IX. Scaling laws for solute diffusion in gels. *J. Appl. Polym. Sci.* **36**, 735–747 (1988).
39. H. P. Erickson, Size and shape of protein molecules at the nanometer level determined by sedimentation, gel filtration, and electron microscopy. *Biol. Proceed. Online* **11**, 32–51 (2009).
40. D. T. Nguyen, B. Jeon, G. R. Abraham, O. A. Saleh, Length-dependence and spatial structure of DNA partitioning into a DNA liquid. *Langmuir* **35**, 14849–14854 (2019).
41. C. P. Goodrich, M. P. Brenner, K. Ribbeck, Enhanced diffusion by binding to the crosslinks of a polymer gel. *Nat. Commun.* **9**, 4348 (2018).
42. B. E. Withers, J. C. Dunbar, Sequence-specific DNA recognition by the SMAI endonuclease. *J. Biol. Chem.* **270**, 6496–6504 (1995).
43. H. C. Berg, *Random Walks in Biology* (Princeton University Press, Princeton, NJ, 1993).
44. H. S. Carslaw, J. C. Jaeger, *Conduction of Heat in Solids* (Clarendon Press, Oxford, UK, 1959).
45. H. B. Schmidt, R. Rohatgi, In vivo formation of vacuolated multi-phase compartments lacking membranes. *Cell Rep.* **16**, 1228–1236 (2016).
46. P. R. Banerjee, A. N. Milin, M. M. Moosa, P. L. Onuchic, A. A. Deniz, Reentrant phase transition drives dynamic substructure formation in ribonucleoprotein droplets. *Angew. Chem.* **56**, 11354–11359 (2017).
47. S. Biffi *et al.*, Equilibrium gels of low-valence DNA nanostars: A colloidal model for strong glass formers. *Soft Matter* **11**, 3132–3138 (2015).